SUPPLEMENTARY INFORMATION

Supplemental Note 1: Bioinformatic analysis of gene expression datasets

Direct Estimation of Extramembrane Bulkiness from Protein Sequences. We performed the following analyses using all of the human-annotated protein isoform sequences contained in the NCBI repository (Refseq release 54). Within each isoform sequence we identified transmembrane helices by fitting a hidden markov model implemented in the TMHMM Server v2.0 (http://www.cbs.dtu.dk/services/TMHMM). As suggested by the authors, we considered any isoform sequences predicted to have more than 18 amino acids in transmembrane helices to be candidate transmembrane proteins unless those amino acids were exclusively within 60 amino acids of the N-terminus (and consequently may correspond to signaling peptides rather than transmembrane domains). Within those isoform sequences predicted to encode membrane proteins, we identified the locations of predicted O-Glycosylation sites within each sequence using the NetOglyc 3.1 program using the default settings (http://www.cbs.dtu.dk/services/NetOGlyc), and predicted the locations of N-glycoslylation sites by searching for the known "(S/T)XN" amino acid sequence motif present at N-glycosylation sites. Next, within each isoform we counted the number of predicted N- and O-glycosylation sites that were present within the portion of the isoform sequence that was predicted to localize to the exterior of the membrane to arrive at isoform-level tallies of external glycosylation sites. Finally, we combined all isoforms annotated to each gene by taking the maximum number of predicted sites of each type across all isoforms to arrive at gene-level summaries of external bulkiness.

In most cases all isoforms annotated to a given gene are highly similar in terms of N- and O-glycosylation site content, and the results of our analyses were robust to the particular method used for combining site tallies across isoforms. We also note that this analysis is unable to differentiate proteins that localize to the extracellular membrane from those present in intracellular (e.g., organelle) membranes, and so our subsequent analyses are likely to be underpowered overall. The analytical pipeline used to estimate bulkiness is depicted in Extended Data Fig. 1a; perl scripts written to perform the above analyses are available upon request from RB.

Association of Transcriptional Changes Observed in Human Tumors with Membrane Protein Bulkiness. We reasoned that increased bulkiness at the cell membrane may play a role in the ability of tumor cells to disseminate and metastasize to distant sites. To test this, we analyzed two publicly available expression microarray data sets characterizing different aspects of tumor dissemination in breast cancer: one characterizing transcription in primary tumors from patients of differing circulating tumor cell status (GEO accession GSE31364), and one comparing transcription in breast tumors that metastasized to diverse sites (GEO accession GSE12276). Specifically, we asked if genes whose products were likely to contribute to membrane bulkiness were disproportionately likely to be transcriptionally upregulated in tumors with clinical evidence for widespread dissemination.

In each dataset, we used one-sided t-tests to quantify the evidence that each gene had elevated expression among patients with detectable CTCs relative to the control group, or among patients with distant relative to local metastatic spread, as appropriate (p-values). In cases where

a gene's expression level was measured with multiple probe sets, we used the minimum p-value calculated among all of the probe sets annotated to the corresponding gene as the gene-level estimate. Then, we partitioned genes into subsets depending on whether the gene was predicted to encode a membrane-bound protein, and if the gene was predicted to have many external N- or O-glycosylation sites. Finally, we compared the distributions of the p-values calculated for all of the genes within each group to the full distribution using a one-sided Kolmogorov-Smirnov test (K-S test).

We empirically determined the cutoffs corresponding to "many" glycosylation sites from the distribution across all predicted membrane-bound proteins. These corresponded to five or more O-glycosylation sites and eleven or more N-glycosylation sites and resulted in the clearest separation of the corresponding classes; we observed similar overall patterns across a range of bulkiness cutoffs, however.

Explained Variance. To determine the extent to which of upregulated gene expression was explainable by gene-level contributions to extramembrane bulkiness, we focused on the set of membrane-associated proteins identified in the above analyses. Specifically, we converted the p-values quantifying evidence for transcriptional upregulation in tumors derived from patients with disseminated disease into Z-scores and then regressed these values on the square roots of the corresponding overall bulkiness measures for each gene (total number of N- and O-glycosylation sites; we regressed on the square root to stabilize the values). We estimated the proportion of the variance explained in each comparison by dividing the residuals from the linear model described above by the residuals obtained by fitting the data to the intercept (no bulkiness term).

Dataset-Level Significance and Test Correction. To empirically estimate the significance of the observed enrichment of upregulated genes with bulky groups within the public data, we iteratively permuted the corresponding p-values across gene labels and calculated the proportion of times that the distributions of p-values in each of the subselected categories were shifted towards zero in a manner consistent with what we observed in the true analysis. Specifically, we counted the number of times that all of the following were true: 1) the one-sided p-value (K-S test) comparing the extracellular group to all genes was equal to or smaller than observed in the experiment, 2) At least one of the one-sided p-values comparing the "many" N- and O-glycosylation groups to the extracellular group was smaller than or equal to either of those observed in the experiment, and 3) the one-sided p-values comparing the group containing genes with many N- and O-glycosylation sites to each of the individual many-site groups were equal to or smaller than those observed in the experiment (e.g., the combined group is more shifted than the individual groups). We performed the permutation 10000 times for each experiment.

Analysis of glycan-modifying enzymes. We performed a similar analysis as those described above to determine whether expression levels of mRNA encoding glycan modifying enzymes is similarly systematically elevated in the CTC and metastasis datasets (Extended Data Fig 1c-e). We assigned genes to each of the indicated sub-categories on the basis of the GLYCOv4 Gene Chip expression microarray annotations provided by the Consortium for Functional Glycomics.

Specifically, we assigned all proteins annotated to the "Glycan Degradation" category to the "Glycosidases" subset (n = 61) and all proteins annotated to the "Glycan-transferase" category to the "Glycosyltransferases" subset (n = 198). Subsets of glycosyltransferases were also considered in unique categories. The Sialyltransferase group contained ST3GAL1, ST3GAL2, ST3GAL3, ST3GAL4, ST3GAL5, ST3GAL6, ST6GAL1, ST6GAL2, ST6GALNAC1, ST6GALNAC2, ST6GALNAC3, ST6GALNAC4, ST6GALNAC5, ST6GALNAC6. The N-acetylgalactosaminyltransferase group consisted of GALNT1, GALNT2, GALNT3, GALNT4, GALNT5, GALNT6, GALNT7, GALNT8, GALNT9, GALNT10, GALNT11, GALNT12, GALNT13, GALNT14, GALNTL1, GALNTL2, GALNTL3, GALNTL4, and GALNTL5. As above, within each dataset we compared the genewise distributions of one-tailed p-values in each subset to the full distribution using a K-S test.

Supplemental Note 2: Computational model

A model describing the mechanics of the cell-ECM interface and the integrated biochemistry of integrin-ligand interaction was built as described previously and summarized here.[1] The cell-ECM interface was modeled as a composite material consisting of a rigid substrate to describe the ECM; a flat, isotropic, elastic plate to describe the plasma membrane and associated cortex; and a uniform, repulsive harmonic potential between the substrate and plate to describe the glycocalyx. The mechanical model of the cell-ECM interface was discretized using a three-dimensional lattice spring model (LSM) whose cross-section is shown in Extended Data Fig. 2. For this configuration of springs, the membrane/cortex plate behaves as an isotropic, elastic solid that has a fixed Poisson's ration (v = 0.25) and a Young's modulus:

$$Y = \frac{5\sigma_m}{2\Delta x} \tag{1}$$

where Δx is the lattice node spacing and σ_m is the membrane/cortex spring constant (Supplemental Table 3). The effective compressibility of the glycocalyx is given by the harmonic potential per unit differential area:

$$G = \frac{\sigma_g}{2\Delta x^2} H(x,y)^2 \tag{2}$$

where H is the local compression of the glycocalyx relative to its equilibrium thickness, l_g, and σ_g is the spring constant describing the compressibility of the glycocalyx (Supplemental Table 3). Integrin-ligands bonds were modeled mechanically as Hookean springs with a spring constant, σ_b, and equilibrium length, l_b (Supplemental Table 3).

Bonds were introduced into the model at a location in the membrane by connecting the nearest node in the membrane-cortex LSM to a node directly underneath in the ECM substrate. The deformations in the model caused by these bonds were calculated by relaxing the entire spring network to equilibrium by minimizing the potential energy of the system, given by:

$$E = \frac{1}{2}\sum_i \sum_j \sigma_{ij}\left(\left|r_{ij}\right| - l_{ij}\right)^2 \tag{3}$$

where the summation i is over all nodes in the system, the summation j is over all nodes connected to node i, $|r_{ij}|$ is the distance between node i and j, and σ_{ij} and l_{ij} are the Hookean constant and equilibrium length of the spring connecting nodes i and j.

Integration of biochemistry and mechanics was achieved using the Bell-model, which describes the distance-dependent bond kinetics for tethered receptor-ligand interactions. The dissociation rate for a bond under force was originally described by Bell[2] and is given by:

$$k_r(F) = k_r^o exp\left(\frac{F\gamma}{k_b T}\right) \tag{4}$$

where k_r^o is the intrinsic unstressed dissociation rate, F is the force on the bond, and γ is the bond's sensitivity to force, termed reactive compliance (Supplemental Table 3). The on-rate for integrin-binding to a position on the ECM substrate followed from the Boltzmann distribution for affinity given by:

$$k_f(F) = k_f^o exp\left(\frac{F\gamma - \Delta E}{k_b T}\right) \tag{5}$$

where k_f^o is the intrinsic unstressed associate rate and ΔE is the minimum mechanical potential energy change resulting from bond formation, calculated using equation 3 (Supplemental Table 3).

The chemo-mechanical model was used to calculate the likelihood of bond formation for different configurations of the cellular glycocalyx, which was manipulated *in silico* by adjusting the spring constants and equilibrium lengths that describe the glycocalyx in the model. To measure integrin-ligand bond rate as a function of distance from a pre-existing adhesion cluster, nine integrin-ligand bonds were added to the center of the plasma membrane and substrate spanning a 3x3 cluster of nodes. The on-rate for a new bond at a defined lateral distance from the cluster was calculated using equation 5.

Parameter	Definition	Value	Ref
σ_g	Glycocalyx spring constant	0.02 pN nm^{-1}	3
σ_m	Membrane spring constant	0.4 pN nm^{-1}	4–6
σ_b	Integrin bond spring constant	2 pN nm^{-1}	7
l_g	Unstressed glycocalyx thickness	30 - 200 nm	
l_b	Unstressed integrin bond length	27 nm	8
k_f^o	Unstressed intrinsic on-rate for integrin-ligand	1x10^5 s^{-1}	9,10
k_r^o	Unstressed intrinsic off-rate for integrin-ligand	0.01 s^{-1}	9,10
γ	Reactive compliance of integrin-ligand bond	0.4 nm	11
Δx	Lattice node spacing	10 nm	1
$k_b T$	Thermal Energy	4.28 pN nm	

Supplemental Table 1 Model parameters for the cell-ECM interface

Supplemental Note 3: Description of Muc1 Constructs

Generation of Muc1 lentiviral vectors. To obtain transcriptionally inducible Muc1, the cDNAs were cloned into the 2nd generation lentiviral vector pLV Puro Tet. pLV Puro Tet was prepared from pLV tTRKRAB (Addgene #12249) by inserting in place of the EEF1α promoter and tTRKRAB transgene, a puromycin resistance gene expression cassette consisting of an SV40 promoter and bovine growth hormone polyadenylation sequence in reverse orientation for selection in transduced cells back to back with the regulatable hybrid hepatamerized Tet operator minimal CMV promoter followed by a central polypurine tract and the multiple cloning site (MCS) from pcDNA3.1+ (Invitrogen).

Full length Muc1 having 42 tandem repeats and a flag tag was excised with EcoRI and HindIII, whose end was made blunt by T4 polymerase fill-in, from MMTV Muc1 Flag[12] and ligated into the PmeI and EcoRI sites of pLV Puro Tet to make pLV Puro Tet Muc1 FL. Similarly, ectodomain truncated Muc1 having its tandem-repeats deleted was prepared by excising with EcoRI and HindIII (made blunt) from MMTV ΔTR[12] and ligating into pLV Puro Tet to make pLV Puro Tet Muc1 ΔTR. To make cytoplasmic-tail deleted Muc1, the Muc1 C-terminus was amplified with PCR using a forward primer (5' – AGCTCTACTGAGAAGAATGCTTTGTC – 3') and a reverse primer that introduced a stop codon proximal to the Muc1 transmembrane domain (5' – GTGTGAATTCCTACTTTCGGCGGCACTGACAGACAGCC – 3'). The PCR product was ligated in place of the Muc1 cytoplasmic tail in pLV Puro Tet Muc1 FL using the PstI and EcoRI restriction sites to create pLV Muc1 ΔCT.

Generation of Muc1 ΔTR strain sensor and control constructs. Cytoplasmic-tail deleted Muc1 ΔCT was excised from pLV Puro and ligated into the BamHI and EcoRI sites of pcDNA3.1 to make the mammalian expression construct pcDNA3.1 Muc1 ΔCT. To make pcDNA3.1 Muc1 ΔTR YFP and pcDNA3.1 Muc1 ΔTR CFP, YFP (VenusA206K) and CFP (mTurq2) were amplified with PCR introducing a 5' BglII site (5' - GGCAAGATCTCGATGGTGAGCAAGGGCGAGGAGCTGTTC - 3') and 3' NcoI site (5' - GGCACCTGGCAGAGGCCTTGTACAGCTCGTCCATGCCGAGAGTGATC - 3') and ligated into the BglII and NcoI sites of pcDNA3.1 Muc1 ΔCT in place of the Muc1 tandem repeats. Following a similar strategy reported for GFP, cysteine 48 and 70 in YFP and CFP were next mutated (C48S, C70M) via site directed mutagenesis to make the cysteine-free expression constructs pcDNA3.1 Muc1 ΔTR cfYFP and pcDNA3.1 Muc1 ΔTR cfCFP.

For constructing pcDNA3.1 Muc1 ΔTR Sensor, a previously reported FRET-based tension sensor module (TS module; Addgene #26021), which had a mTFP1 and VenusA206K FRET pair separated by an elastic linker, was modified by substituting mTurq2 for mTFP1[13]. The TS module was first amplified with PCR using a forward primer (5' – GGCAGAATGCCATGGTGAGCAAGGGCGAGGAGACCACA – 3') and a reverse primer (5' – GGCAGCGGCCGCATCCATGGGCCTTATACAGCTCGTCCA TGCCGAGAGTGATCCC – 3') that removed the Venus BsrGI restriction site and stop codon and added 3' NcoI and NotI restriction sites. mTurq2 was also amplified with a forward primer that introduced 5' EcoRI and BglII restriction sites (5' –

GGCAGAATTCATAGATCTCGATGGTGAGCAAGGGCGAGGAG - 3') and a reverse primer (5' – CAAATGTGGTATGGCTGATTATGATC – 3'). The TS module product was digested with BsrGI and NotI and the mTurq2 product digested with EcoRI and BsrGI. These fragments were subsequently ligated together into the EcoRI and NotI sites of pcDNA3.1 to make pcDNA3.1 mTurq2 TS module. To make pcDNA3.1 Muc1 ΔTR Sensor, the mTurq2 TS module was excised with BglII and NcoI and ligated into the BglII and NcoI sites of pcDNA3.1 Muc1 ΔCT in place of the Muc1 tandem repeats. Finally, to make the cysteine-free sensor construct, the VenusA206K cysteines were mutated (C48S, C70M) via site directed mutagenesis. Next mTurq2 was replaced with the cysteine free mTurq2 from pcDNA3.1 Muc1 ΔTR cfCFP using the BamHI and BsrGI restriction sites in each construct to make pcDNA3.1 Muc1 ΔTR cfSensor.

For construction of the sensor and control constructs with a full-length ectodomain, the NcoI sites of Muc1 ΔTR cfYFP and Muc1 ΔTR cfCFP were destroyed by site directed mutagenesis. To make pcDNA3.1 Muc1 FL cfYFP and pcDNA3.1 Muc1 FL cfCFP, the fluorescent protein and Muc1 C-terminus was amplified from pcDNA3.1 Muc1 ΔTR cfYFP and pcDNA3.1 Muc1 ΔTR cfCFP with PCR using a forward primer that introduced a NcoI site on the 5' end of the fluorescent protein (5' – GGCAATCACATGTAGGTATGGTGAGCAAGGGCGAGGAGCTGTTC - 3') and a reverse primer (5' – GGGAGTGGCACCTTCCAGGGTCA - 3') complementary to the pcDNA polyA tail. The PCR products were ligated into the NcoI and EcoRI sites of pcDNA3.1 Muc1 ΔCT in place of the Muc1 C-terminus to create constructs with full-length Muc1 ectodomains. To make pcDNA3.1 Muc1 FL cfSensor, the truncated Muc1 ectodomain and CFP of pcDNA3.1 Muc1 ΔTR cfSensor was swapped with the full-length ectodomain and CFP from pcDNA3.1 Muc1 FL cfCFP using the BamHI and BsrGI restriction sites. The protein product of the full-length Muc1 FRET sensor construct was comparable in size to Muc1 and had similar effects on cell adhesion (Extended Data Fig. 7a).

Generation of Muc1 C-terminus fusions with mEmerald and mEos2. To construct a full-length Muc1 C-terminal fusion with mEmerald, the N-terminal ectodomain of Muc1 was excised from pLV Puro Muc1 FL with XhoI and ApaLI and the Muc1 C-terminus was amplified via PCR with a forward primer (5' – GCCTCAGGCTCTGCATCAGGCTCAG- 3') and a reverse primer that simultaneously removed the Muc1 stop codon and introduced a ApoI restriction site (5' – GTGTGAATTTCCAAGTTGGCAGAAGTGGCTGCCACT – 3'). The ApaLI/ApoI digested PCR product along with XhoI/ApaLI N-terminal ectodomain were ligated into the XhoI/EcoRI restriction sites of mEmerald N1 to make Muc1 FL mEmerald. A fusion of mEmerald with a truncated Muc1 cytoplasmic tail was prepared with a similar strategy. The C-terminus of Muc1 in pLV Puro Tet Muc1 ΔCT was amplified with a forward primer (5' - GCCTCAGGCTCTGCATCAGGCTCAG - 3') and reverse primer (5' – GTGTGAATTTCCTTTCGGCGGCACTGACAGACAGCC - 3'). The ApaLI/ApoI digested PCR product along with XhoI/ApaLI N-terminal ectodomain were ligated into the XhoI/EcoRI restriction sites of mEmerald N1 to make Muc1 ΔCT mEmerald. Fusions with mEos2 were prepared with an identical strategy, using mEos2 N1 in place of mEmerald N1 to make Muc1 FL mEos2 and Muc1 ΔCT mEos2.

Additional constructs., Paxillin-mCherry, Vinculin-mCherry, CAAX-mCherry, and pBabepuro3 vSrc:ER vectors were described previously[14,15].

Supplemental Note 4: Acceptor Photobleaching FRET

FRET methodology and controls: For measuring the FRET efficiency of the Muc1 FRET sensor constructs, the acceptor photobleaching FRET (pbFRET) methodology was implemented on a spinning disk confocal microscope, which enabled imaging of Muc1 in the dorsal and ventral plasma membrane. On our optical setup, axial chromatic aberration limited the reliability of the standard three-cube FRET method, which requires quantitative comparison of CFP and YFP intensities. The pbFRET was instead implemented, since it requires imaging only a single color channel, CFP, before and after bleaching the YFP acceptor. Complete details of the pbFRET methodology and protocols have previously been published[16].

The major sources of artifacts in pbFRET measurements were controlled for (Extended Data Fig 7b-d). First, we recorded similar FRET ratios when expressing different levels of our sensor construct, indicating that background intensity in images was correctly accounted for (Extended Data Fig. 7b). Second, we detected minimal CFP photobleaching between imaging cycles (Extended Data Fig. 7c). Third, we ruled out intermolecular FRET as a major source of our FRET signal by co-expressing Muc1 YFP and Muc1 CFP to similar levels on the cell surface (Extended Data Fig. 7d). FRET between these molecules was small compared to intramolecular FRET measured when expressing the CFP-YFP sensor. Finally, we determined that YFP was almost fully bleached during our 10 second bleaching cycle with the 515 nm laser line.

Supplemental Note 5: sptPALM Analysis

A typical sptPALM experiment leads to a set of 20,000 images per cell analyzed in order to extract molecule localization and dynamics. Single molecule fluorescent spots were localized and tracked over time using a combination of wavelet segmentation and simulated annealing algorithms[17–19]. Under the experimental conditions described above, the resolution of the system was quantified to 47 nm (Full Width at Half Maximum, FWHM). This spatial resolution depends on the image signal to noise ratio and the segmentation algorithm and was determined using fixed mEos2 samples[20]. We analyzed 130 2D distributions of single molecule positions belonging to long trajectories (>50 frames) by bi-dimensional Gaussian fitting, the resolution being determined as 2.3 σ_{xy}, where σ_{xy} is the pointing accuracy. For the trajectory analysis, focal adhesions and Muc1 rich areas were identified by wavelet image segmentation of the paxillin-GFP or Muc1-GFP, respectively. The corresponding binary mask was used to sort single particle data analyses to specific regions.

We analyzed trajectories lasting at least 20 points (≥400 ms) with a custom routine written for Matlab using the mean squared displacement MSD computed as (equation 1):

$$MSD(t = n \cdot \Delta t) = \frac{\sum_{i=1}^{N-n}(x_{i+n}-x_i)^2+(y_{i+n}-y_i)^2}{N-n} \qquad (1)$$

where x_i and y_i are the coordinates of the label position at time $i \cdot \Delta t$. We defined the measured diffusion coefficient D as the slope of the affine regression line fitted to the $n = 1$ to 4 values of the $MSD(n \cdot \Delta t)$. The MSD was computed then fitted on a duration equal to 60% (minimum of 12 points, 240 ms) of the whole stretch by (equation 2):

$$MSD(t) = \frac{4r_{conf}^2}{3}\left(1 - e^{-t/\tau}\right) \qquad (2)$$

where r_{conf} is the measured confinement radius and τ the time constant ($\tau = r_{conf}^2/3D_{conf}$). Trajectories were sorted in 3 groups: immobile, confined diffusion and free-diffusion. Immobile trajectories were defined as trajectories with D<0.008 µm².s⁻¹, corresponding to molecules which explored an area inferior to the one defined by the image spatial resolution ~(0.05µm)² during the time used to fit the initial slope of the MSD (4 points, 80 ms): D$_{threshold}$=(0.05µm)²/(4x4x0.02s)~0.008 µm².s⁻¹ [21]. To separate trajectories displaying free-diffusion from confined diffusion, we used the time constant τ calculated for each trajectory. Confined and free-diffusing trajectories were defined as trajectories with a time constant τ respectively inferior and superior to half the time interval used to compute the MSD (120 ms).

To analyze the number of mEos2-fused β3 integrins crossing the boundaries of Muc1-rich areas, we used a custom routine written in C++ to sort trajectories inside, outside, and those leaving or entering Muc1-rich areas. Leaving trajectories were defined as trajectories starting in a Muc1-rich area and ending outside, and reciprocally for entering trajectories. The number of crossing integrins (expressed in trajectories/µm) depends on the level of mEos2-integrin expression, and on the level of mEos2 photo-activation. To compare the relative number of integrins crossing, we normalized it by the number of integrins crossing fictive boundaries drawn within Muc1-rich areas of the corresponding cell (see Extended Data Fig. 6).

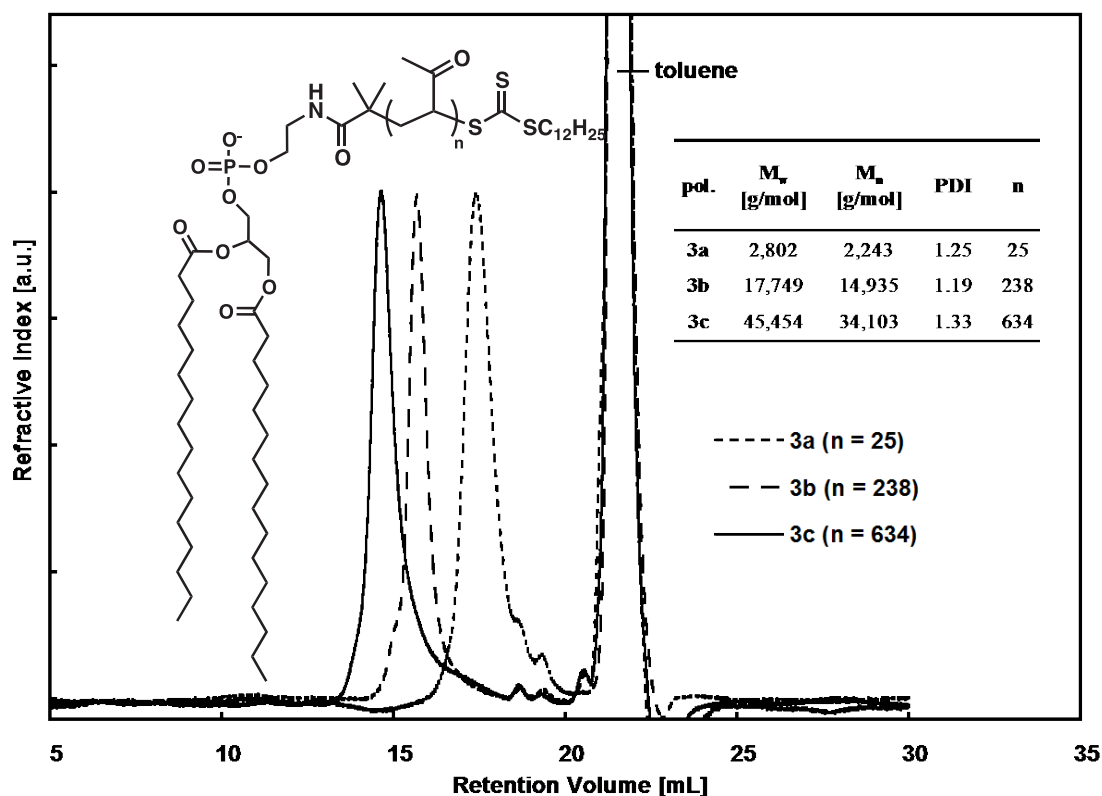## Supplemental Note 6: Glycomimetic synthesis

General procedures: Lipid-terminated mucin mimetics mono-functionalized with Alexa Fluor 488 (AF488) were synthesized according to previously published procedures[22]. The synthesis is described in detail below and summarized in Extended Data Fig 3a. All chemicals, unless stated otherwise, were purchased from Sigma-Aldrich. Alexa Fluor 488-C_5-maleimide was purchased from Invitrogen. Methylvinyl ketone (MVK, 1) and 2-butanone were freshly distilled prior to polymerization. Chain transfer agent (2) and α-aminooxy-GalNAc (5) were synthesized according to previously published procedures[22,23]. Solvents were purified on a Glass Contour solvent purification system. Nuclear magnetic resonance (NMR) spectra were recorded on a Bruker Biospin Advance II 500 MHz High Performance NMR spectrometer with multinuclear CP-MAS probe. Spectra were recorded in $CDCl_3$ or D_2O solutions at 293 K and referenced to residual solvent peaks. Size exclusion chromatography (SEC) was performed on Shimadzu LC-20AD Prominence Liquid Chromatograph with Viscotek VE 3580 RI detector. For SEC measurements in DMF (0.2% LiBr), the instrument was equipped with two in-series mixed bed GMHHR-M columns, separation range 100-4M (30 cm x 7.8 mm i.d.) at 70 °C. UV-VIS spectra were collected on a Perkin Elmer Lambda 35 UV/VIS spectrometer.

RAFT polymerization of MVK (1)[24,25] in the presence of lipid-containing chain transfer agent 2. A flame-dried Schlenk flask (10 mL) equipped with a magnetic stirring bar was charged with chain transfer agent (CTA, 2), ACVA (4,4'-azobis(4-cyanovaleric acid), and MVK (1) according to stoichiometric ratios listed in Supplemental Table 4. An amount of 2-butanone was added to give a 50 wt% solution of 1. The flask was equipped with a rubber septum and attached to a Schlenk line. The yellow solution was degassed by three freeze-pump-thaw cycles. After the final cycle, the flask was back-filled with N_2, allowed to warm to room temperature and immersed into an oil bath preheated to 65 °C. After 16.5 h, the reaction mixture was diluted with DCM and precipitated by the addition into hexanes. The residue was re-dissolved in a minimal quantity of DCM and precipitated again by the addition into hexanes with vigorous stirring. This was repeated twice more. The yellow polymer was concentrated from chloroform three times to remove residual hexanes and dried under high vacuum overnight to give polymers 3 as pale yellow solids. Yields of polymers 3 and their characterization data are summarized in Supplemental Table 4. SEC traces for all three polymers are shown in Supplemental Figure 1. ^{1}H NMR spectra for polymers 3 are shown in Supplemental Figure 2.
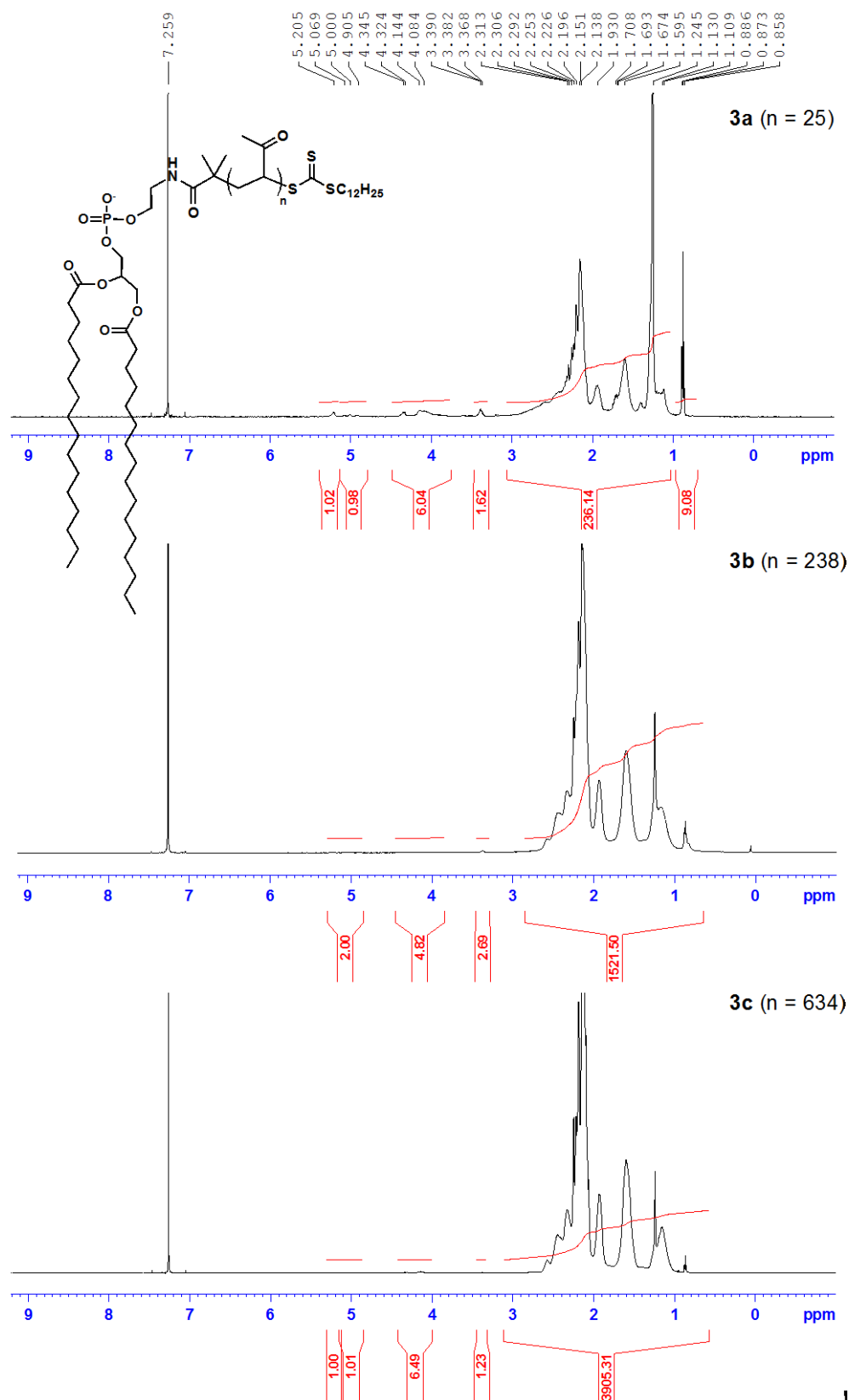
Synthesis of lipid-terminated poly(MVK) polymers with free thiol functionality (4a-c). Each of pMVK polymers 3 (0.004 mmol) was dissolved in DMF (1.5 mL, c_{pol} = 2.4 mM) in a 20-mL scintillation vial equipped with a magnetic stir bar and a septum. To each yellow solution degassed by three freeze-pump-thaw cycles, was added cysteamine solution (free base in DMF, c = 632 mM, 0.018 mmol, 29 µL, 5 equiv. per trithiocarbonate group) under N_2. The reaction was stirred at rt for 20 min. The solution turned colorless and ether (15 mL) was added. The collected polymers 4a-c were dissolved in a small amount of chloroform and precipitated by the addition of hexanes. This was repeated twice more and the final white solids were dried under vacuum overnight. The reaction afforded polymers 4 as white solids in a quantitative yield. SEC and ^{1}H NMR data for polymers 4 are shown in Supplemental Figures 3 and 4, respectively.

Synthesis of AF488-labeled mucin mimetics (6a-c). The free thiol-terminated intermediates 4 were dissolved in DMF in 4-mL vials equipped with a magnetic stir bar to give solutions with a final thiol concentration of 1 mM. An aliquot of AF488-maleimide solution in DMF (c = 2mM, 2 equiv. per thiol group) was added to each polymer. The solutions were degassed and allowed to stir under N_2 at room temperature for 18 hr. After this time, the reactions were diluted with DCM and precipitated by the addition of hexanes. The crude AF488-labeled polymer backbones (1.0 mg) were dissolved in THF (50 µL) and transferred into Eppendorf tubes containing an aliquot of a solution of α-aminooxy-GalNAc (5, 47.6 µL, c = 330 mM, 1.1 equiv. per keto group) in acetate buffer (100 mM, pH = 5.5). The tubes were placed in a heating block set at 50 °C for 12 hrs. After this time, the solvents were removed and additional acetate buffer (50 µL) was added. The tubes were heated at 50 °C for additional 18 hr. The crude reaction mixtures were loaded onto a Sephadex G-25 (PD-10) desalting column. The polymers were eluted with DI water and the collected fractions were lyophilized to give orange polymers 6a-c. Isolated yields and the efficiencies of AF488-labeling and GalNAc ligation are summarized in Supplemental Table 5. The extent of polymer labeling with AF488 was determined based on absorbance at λ_{max} = 550 nm (UV-Vis spectra for polymers 6 are shown in Supplemental Figure 5). Efficiency of GalNAc ligation was determined by ^{1}H NMR analysis as shown in Supplemental Figure 6. The lengths of fully extended polymers 6a-c were estimated as described previously[22].
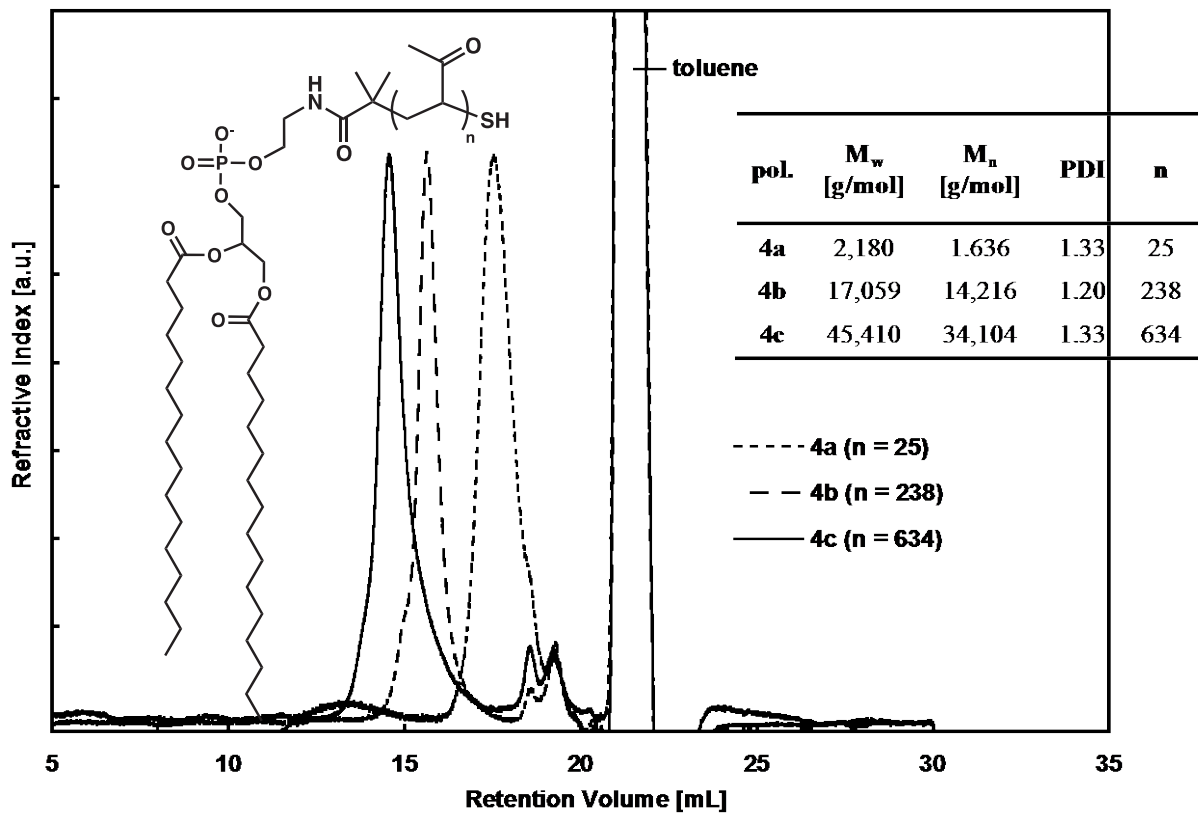

pol.	M_w [g/mol]	M_n [g/mol]	PDI	n
3a	2,802	2,243	1.25	25
3b	17,749	14,935	1.19	238
3c	45,454	34,103	1.33	634

- - - - - 3a (n = 25)
— — 3b (n = 238)
——— 3c (n = 634)

Supplemental Figure 1 SEC traces and characterization for polymers 3a-c.

Supplemental Figure 2 ^{1}H NMR spectra of polymers 3a-c.

pol.	M_w [g/mol]	M_n [g/mol]	PDI	n
4a	2,180	1.636	1.33	25
4b	17,059	14,216	1.20	238
4c	45,410	34,104	1.33	634

- - - - 4a (n = 25)
— — 4b (n = 238)
—— 4c (n = 634)

Supplemental Figure 3 SEC traces and characterization for polymers 4a-c.

Supplemental Figure 4 ^{1}H NMR spectra of polymers 4a-c.
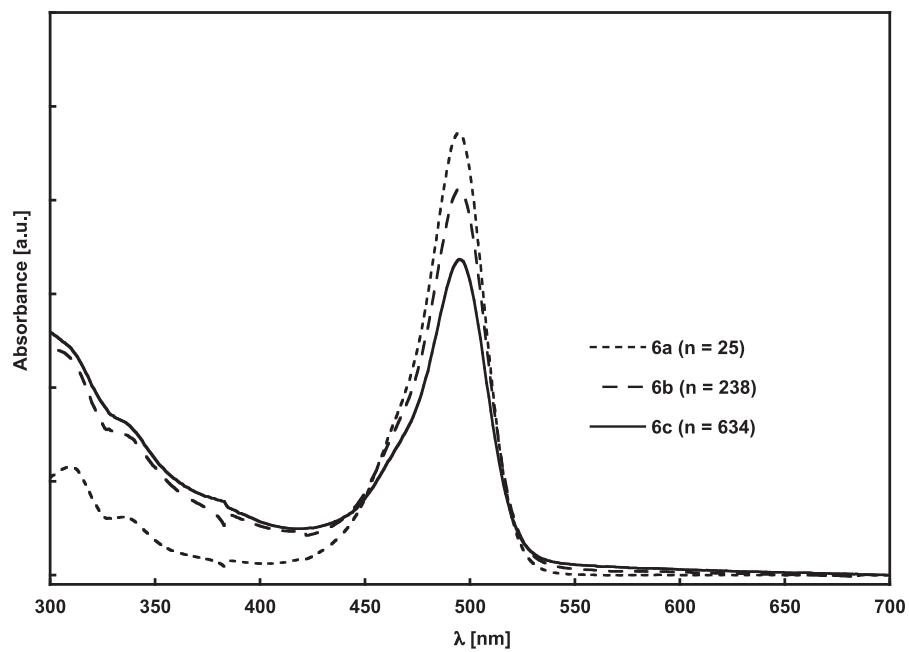
Supplemental Figure 5 UV-VIS spectra of polymers 6a-c.
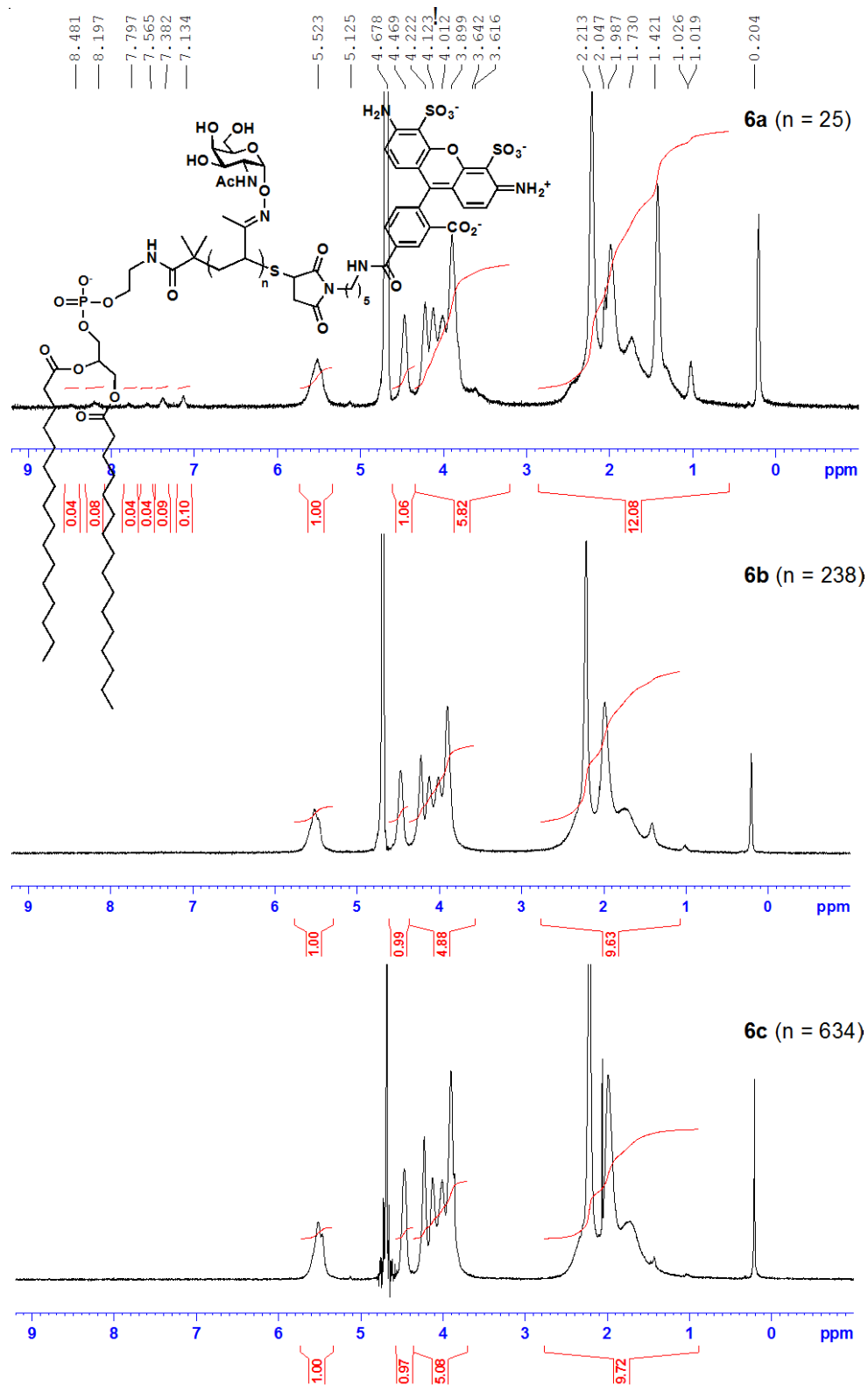
Supplemental Figure 6 ^{1}H NMR spectra of polymers 6a-c.

1. Paszek, M. J., Boettiger, D., Weaver, V. M. & Hammer, D. A. Integrin clustering is driven by mechanical resistance from the glycocalyx and the substrate. *PLoS Comput Biol* **5,** e1000604 (2009).

2. Bell, G. I. Models for the specific adhesion of cells to cells. *Science* **200,** 618–627 (1978).

3. Agrawal, N. J. & Radhakrishnan, R. The Role of Glycocalyx in Nanocarrier-Cell Adhesion Investigated Using a Thermodynamic Model and Monte Carlo Simulations. *J. Phys. Chem. C Nanomater. Interfaces* **111,** 15848–15856 (2007).

4. Charras, G. T., Coughlin, M., Mitchison, T. J. & Mahadevan, L. Life and times of a cellular bleb. *Biophys. J.* **94,** 1836–1853 (2008).

5. Feneberg, W., Aepfelbacher, M. & Sackmann, E. Microviscoelasticity of the apical cell surface of human umbilical vein endothelial cells (HUVEC) within confluent monolayers. *Biophys. J.* **87,** 1338–1350 (2004).

6. Hwang, W. C. & Waugh, R. E. Energy of dissociation of lipid bilayer from the membrane skeleton of red blood cells. *Biophys. J.* **72,** 2669–2678 (1997).

7. Caputo, K. E. & Hammer, D. A. Effect of microvillus deformability on leukocyte adhesion explored using adhesive dynamics simulations. *Biophys. J.* **89,** 187–200 (2005).

8. Nermut, M. V., Green, N. M., Eason, P., Yamada, S. S. & Yamada, K. M. Electron microscopy and structural model of human fibronectin receptor. *EMBO J.* **7,** 4093–4099 (1988).

9. Luo, B.-H., Strokovich, K., Walz, T., Springer, T. A. & Takagi, J. Allosteric beta1 integrin antibodies that stabilize the low affinity state by preventing the swing-out of the hybrid domain. *J. Biol. Chem.* **279,** 27466–27471 (2004).

10. Takagi, J., Erickson, H. P. & Springer, T. A. C-terminal opening mimics 'inside-out' activation of integrin alpha5beta1. *Nat. Struct. Biol.* **8,** 412–416 (2001).

11. Li, F., Redick, S. D., Erickson, H. P. & Moy, V. T. Force measurements of the alpha5beta1 integrin-fibronectin interaction. *Biophys. J.* **84,** 1252–1262 (2003).

12. Schroeder, J. A., Thompson, M. C., Gardner, M. M. & Gendler, S. J. Transgenic MUC1 interacts with epidermal growth factor receptor and correlates with mitogen-activated protein kinase activation in the mouse mammary gland. *J. Biol. Chem.* **276,** 13057–13064 (2001).

13. Grashoff, C. *et al.* Measuring mechanical tension across vinculin reveals regulation of focal adhesion dynamics. *Nature* **466,** 263–266 (2010).

14. Paszek, M. J. *et al.* Scanning angle interference microscopy reveals cell dynamics at the nanoscale. *Nature methods* **9,** 825–7 (2012).

15. Aziz, N., Cherwinski, H. & McMahon, M. Complementation of defective colony-stimulating factor 1 receptor signaling and mitogenesis by Raf and v-Src. *Mol. Cell. Biol.* **19,** 1101–1115 (1999).

16. Kenworthy, A. K. Imaging protein-protein interactions using fluorescence resonance energy transfer microscopy. *Methods San Diego Calif* **24,** 289–296 (2001).

17. Racine, V. *et al.* Multiple-target tracking of 3D fluorescent objects based on simulated annealing. in *3rd IEEE Int. Symp. Biomed. Imaging Nano Macro 2006* 1020–1023 (2006). doi:10.1109/ISBI.2006.1625094

18. Racine, V. *et al.* Visualization and quantification of vesicle trafficking on a three-dimensional cytoskeleton network in living cells. *J. Microsc.* **225,** 214–228 (2007).

19. Izeddin, I. *et al.* Wavelet analysis for single molecule localization microscopy. *Opt. Express* **20,** 2081–2095 (2012).

20. Cheezum, M. K., Walker, W. F. & Guilford, W. H. Quantitative comparison of algorithms for tracking single fluorescent particles. *Biophys. J.* **81,** 2378–2388 (2001).

21. Tardin, C., Cognet, L., Bats, C., Lounis, B. & Choquet, D. Direct imaging of lateral movements of AMPA receptors inside synapses. *EMBO J.* **22,** 4656–4665 (2003).

22. Godula, K. *et al.* Control of the molecular orientation of membrane-anchored biomimetic glycopolymers. *J. Am. Chem. Soc.* **131,** 10263–10268 (2009).

23. Marcaurelle, L. A., Shin, Y., Goon, S. & Bertozzi, C. R. Synthesis of oxime-linked mucin mimics containing the tumor-related T(N) and sialyl T(N) antigens. *Org. Lett.* **3,** 3691–3694 (2001).

24. Moad, G., Rizzardo, E. & Thang, S. H. Living radical polymerization by the RAFT process–a second update. *Aust. J. Chem.* **62,** 1402–1472 (2009).

25. Cheng, C., Sun, G., Khoshdel, E. & Wooley, K. L. Well-defined vinyl ketone-based polymers by reversible addition-fragmentation chain transfer polymerization. *J. Am. Chem. Soc.* **129,** 10086–10087 (2007).